

PAPER

Divertor impurity seeding experiments at the COMPASS tokamak

To cite this article: M. Komm *et al* 2019 *Nucl. Fusion* **59** 106035

View the [article online](#) for updates and enhancements.

Recent citations

- [Kinetic modeling of seeded nitrogen in an ITER baseline scenario](#)
F Schluck
- [Impact of impurity seeding on the electron energy distribution function in the COMPASS divertor region](#)
M Dimitrova *et al*
- [SOLPS analysis of the necessary conditions for detachment cliff](#)
Hailong Du *et al*








IOP | ebooks™

Bringing together innovative digital publishing with leading authors from the global scientific community.

Start exploring the collection—download the first chapter of every title for free.

Divertor impurity seeding experiments at the COMPASS tokamak

M. Komm¹, I. Khodunov^{1,2}, J. Cavalier¹, P. Vondracek^{1,3}, S. Henderson⁴ , J. Seidl¹, J. Horacek¹ , D. Naydenkova¹, J. Adamek¹, P. Bilkova¹, P. Bohm¹, A. Devitre², M. Dimitrova^{1,5}, S. Elmore⁴, M. Faitsch⁶ , P. Hacek^{1,3}, J. Havlicek¹, A. Havranek¹, M. Imrisek^{1,3}, J. Krbec¹ , M. Peterka^{1,3} , R. Panek¹, O. Samoylov², M. Sos¹, M. Tomes^{1,3}, K. Tomova², V. Weinzettl¹ and The EUROfusion MST1 Team^a

¹ Institute of Plasma Physics of the CAS, Za Slovankou 3, 182 00 Prague 8, Czech Republic

² Department of Applied Physics, Gent University, Gent, Belgium

³ Charles Univ, Fac Math & Phys, V Holesovickach 2, 180 00 Prague 8, Czech Republic

⁴ Culham Sci Ctr, CCFE, Abingdon OX14 3DB, Oxon, United Kingdom of Great Britain and Northern Ireland

⁵ Emil Djakov Institute of Electronics, Bulgarian Academy of Sciences, 72, Tsarigradsko Chaussee, 1784 Sofia, Bulgaria

⁶ Max-Planck-Institut für Plasmaphysik, 85748 Garching b. München, Germany

E-mail: komm@ipp.cas.cz

Received 7 January 2019, revised 20 June 2019

Accepted for publication 22 July 2019

Published 4 September 2019



Abstract

Partial detachment is the desired regime for the baseline burning plasma scenario in ITER and other next-step devices, as it allows for the dissipation of the majority of the energy carried by charged particles through the scrape-off-layer and thus avoids localised heat flux deposition in the divertor region. The COMPASS tokamak is equipped with an open divertor and has a relatively short connection length, both factors being unfavourable for access to detachment. As such, it only allows for the approach to naturally detached operation at very high line-averaged densities ($>10^{20} \text{ m}^{-3}$), which are incompatible with maintaining the ELMy H-mode regime. In order to achieve detachment at lower densities, impurities (such as nitrogen) must be injected into the plasma in the divertor region.

A series of experiments with impurity injection in the range of $1\text{--}9 \times 10^{20}$ molecules per second at different locations in the divertor were performed with the aim being to cool the plasma and influence particle and heat transport onto the divertor targets and provoke partial detachment. Previously reported results (Komm *et al* 2017 *Proc. of the 44th EPS Conf.* P1.118) were largely extended by injection of nitrogen at the outer divertor target.

In order to analyze the divertor heat flux footprint in seeded plasmas, the buffered heat flux q_B was introduced, with the radial profile being approximated by an exponential decay. A new set of generic parameters—the peak heat flux q_{peak} , the fraction of power reaching the target f_{div} and divertor footprint spreading factor S_f —were proposed to characterise the divertor footprint under detached conditions.

Keywords: tokamak, detachment, nitrogen, nuclear fusion, divertor

(Some figures may appear in colour only in the online journal)

^a See the author list of [44].

1. Introduction

The power exhaust in the divertor represents one of the key challenges of contemporary fusion research, as the heat fluxes in machines with burning plasmas, such as ITER or DEMO, can easily exceed the material limits of the plasma-facing components (PFCs) and lead to their damage and reduced lifespan [14]. Most of the heat flux escaping from the last closed flux surface (LCFS) is carried along the field lines until it reaches the PFCs in the divertor. To overcome the issue of the divertor overheating in ITER, the partially detached regime is envisaged as the baseline scenario for burning plasmas [15]. Detachment allows for the conversion of a majority of the energy carried by charged particles into radiation and as such prevents the localised deposition of the heat fluxes [16]. It is characterised by an electron temperature gradient along the field lines, as they pass from the scrape-off layer (SOL, upstream) to the divertor target (downstream) and significant power loss in the SOL. The temperature at the target is typically low (<5 eV), allowing a significant population of neutrals to form in the divertor region.

In general, there are two ways to achieve the detached regime—(i) by increasing the density until a sufficient number of collisions with charged and neutral particles leads to power dissipation and cooling of the downstream plasma, or (ii) by injection of selected impurities, often strong radiators, which also allows for the removal of power by radiation. In this work, we will focus on the latter approach, and we will present results of impurity seeding experiments at the COMPASS tokamak, where access to detached operation is particularly difficult due to the open divertor geometry and relatively short connection length. On the other hand, COMPASS has an ITER-like plasma shape and as such it can contribute to improving or formulating the relevant multi-machine scalings.

The physics of detachment is incredibly complex, including atomic physics, surface geometries and plasma-wall interactions. The aim of this contribution is to characterise the practical aspects of detachment, such as the reduction of plasma pressure and heat fluxes in the divertor. In order to do this, we introduce a novel set of generic parameters: peak divertor heat flux q_{peak} , fraction of power reaching the divertor f_{div} and divertor footprint spreading factor S_f , which are able to describe the important properties of virtually any profile, independently of the underlying physics processes.

2. Experimental setup

2.1. Injection scenario

The impurity was injected in a series of otherwise identical attached ohmically heated low confinement mode discharges ($I_p = -210$ kA, $B_T = -1.38$ T, $n_e = 5 \times 10^{19} \text{ m}^{-3}$), as shown in figure 1. After a series of comparative experiments with nitrogen and neon seeding, nitrogen was selected as a more favourable impurity (as it allows for a range of effects in the divertor without the risk of disruptions) and so all the experiments in this work refer to discharges with nitrogen seeding. The impurity particle flux was controlled by a pre-set waveform

on a piezoelectric valve in the range of $1\text{--}9 \times 10^{20}$ molecules per second. A typical waveform included a 10 ms pre-puff during which the valve was requested to be fully opened (to ensure that the valve mechanism starts to function properly), followed by a 100 ms constant puff at the desired particle flux (see figure 1(B)), which was varied on a shot-to-shot basis. Two different seeding locations were used: at first nitrogen injection at the high field side (HFS) in the inner target (major radius $R = 469$ mm) [1], later at the low field side (LFS) in the outer target ($R = 500$ mm), located outside the outer strike point. An example of electron temperature T_e time evolution from the probe set #33 (located at $R = 490.6$ mm, meaning 10 mm outside the outer strike point) is shown in figure 1(D). For reference in the future sections, we include the list of performed discharges in the summary table 1.

2.2. Influence of nitrogen content on probe measurements

Divertor probes are the principal diagnostic systems for detachment studies at COMPASS. In the following analysis, we employ the combined array of 55 Ball-pen probes (BPPs) and 110 Langmuir probes (LPs) (in two linear arrays), which allows for fast ($\sim \mu\text{s}$) measurements of electron temperature T_e , ion saturation current I_{sat} and floating potential V_{float} [2]. This technique has been validated in upstream measurements against Thomson scattering in COMPASS and AUG [3] and in selected cases also against the swept LP of the same divertor probe array [2]. More recently, a comparison with measurements of the divertor infra-red thermography system [41] was also performed (in attached plasma conditions), yielding good agreement. However, a comparison with the array of 39 divertor swept LPs located at different toroidal location [43] did not bring satisfactory agreement, especially in terms of T_e . This disagreement is a subject of ongoing research, however it is clearly outside the scope of this work. Note that T_e measurements of the probe array in the far SOL or during nitrogen seeding, when T_e is low (below 5 eV), could not be validated against other diagnostics in COMPASS due to their insufficient operating range—infrared cameras have difficulties resolving very low heat fluxes [4] and swept probes are known to over-estimate T_e in such conditions [5, 6]. However, it has been shown that BPPs retain their operating properties even at low T_e (see figure 4 in [3]).

The analysis of probe measurements in tokamaks is usually based on an assumption that the plasma consists of a single ion species. This can be clearly violated in the case where there is intensive injection of nitrogen in deuterium plasmas. Unfortunately, it was not possible to determine the fraction of nitrogen ions at the location of probe measurements. However, we can model the effect of variable fractions of nitrogen in the plasma and hence estimate the error which would be made by neglecting the presence of nitrogen in the analysis. In order to do that, we assume that the nitrogen is only singly ionized (which corresponds to the most probable state of nitrogen in the range of temperatures measured during the seeding phase) and we introduce the nitrogen density fraction $f_N = n_N/n_i$. We further assume that the only effect of nitrogen is the presence of an ion current carried by nitrogen ions to the probes,

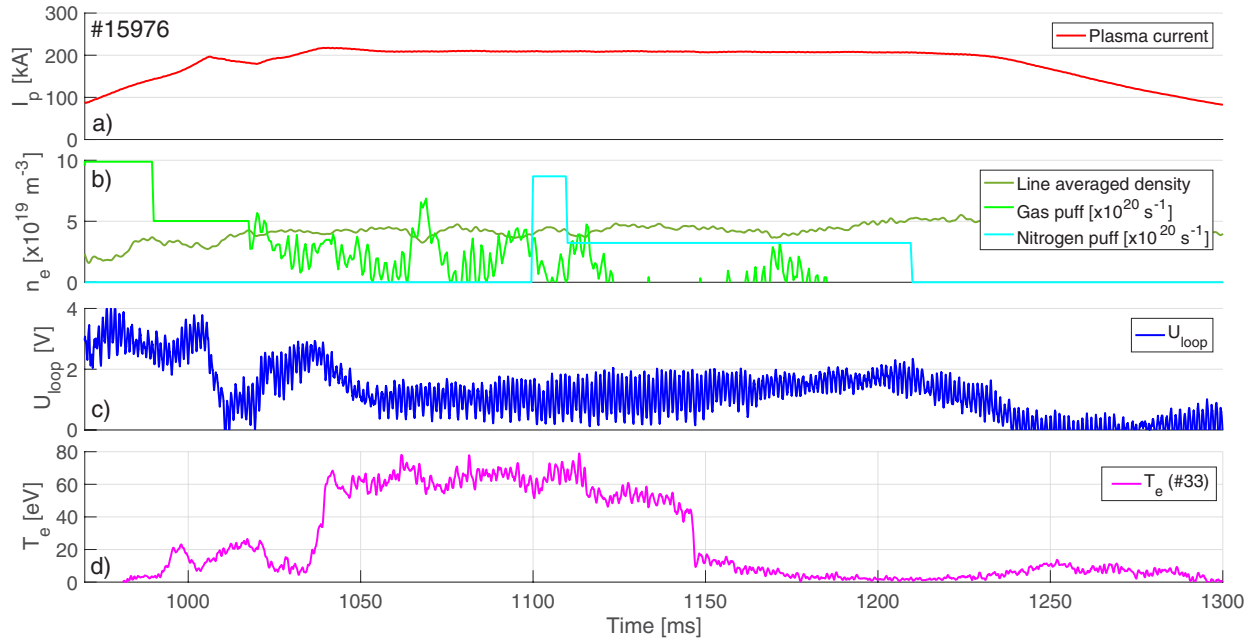


Figure 1. Overview of discharge #19576 with nitrogen injected at the LFS target with profile of plasma current (A), line averaged density (B), loop voltage (C) and electron temperature recorded by probe set #33 ($R = 490.6$ mm) at the LFS target.

omitting the possible effects on ion collecting area, collisional effects in the sheath etc.

The temperature measurements are achieved using a combination of the floating potentials of the BPPs and a LPs, with the knowledge of a coefficient α_{LP} [2]. The value of the LP floating potential is influenced by the presence of nitrogen ions and scales as

$$V_{fl} \sim \ln \left((1 - f_N) \sqrt{m_D/m_e} + f \sqrt{m_N/m_e} \right) / \ln(\sqrt{m_D/m_e}), \quad (1)$$

where m_D and m_N are the deuterium and nitrogen mass respectively. In the absence of a working theoretical model for the BPP, we assume that coefficient α_{BPP} scales equally. This means that the total coefficient $\alpha = \alpha_{LP} - \alpha_{BPP}$ increases with the increasing amount of nitrogen in the plasma. Since the dependence is logarithmic, only small variations of T_e occur within the range of expected nitrogen fractions ($f_N < 20\%$) as shown in figure 2. The classical method of electron temperature extraction from swept LPs is not affected, as it operates with a ratio $I(V)/I_{sat}$, where I_{sat} is also determined experimentally and so it reflects the plasma conditions correctly.

A similar effect occurs when density is extracted from the measurements of ion saturation current. In this case the effective mass influences the ion sound speed and so the density scales as $\sim 1 / (1 - f + f \sqrt{m_D/m_N})$ (shown in figure 2(B)).

Finally, when these two influences are combined, the resulting error in electron pressure and heat flux measurement is shown in figures 2(C) and (D) respectively. Deviations from optimal measurements are observed, however the scale of introduced error is acceptable even for relatively large ($\sim 20\%$) concentrations of nitrogen for the technique employed in further analysis, as well as for the classical method, shown here for reference.

Table 1. List of discharges performed with LFS and HFS nitrogen seeding.

Discharge	HFS seeding		LFS seeding	
	Γ_{N_2} (s^{-1})	Discharge	Γ_{N_2} (s^{-1})	Discharge
—		#15972	1.4×10^{20}	
#13729	2.0×10^{20}	#15973	2.0×10^{20}	
#13725	2.8×10^{20}	#15975	2.6×10^{20}	
#13730	3.7×10^{20}	#15976	3.2×10^{20}	
#13731	4.5×10^{20}	#15977	4.4×10^{20}	

2.3. Upstream measurements

With respect to the upstream measurements, the major source of error is the determination of the location of the LCFS. Since the low-density plasmas in COMPASS are in the sheath-limited regime, it is not possible to determine the separatrix temperature from the power balance as in larger machines [10]. Instead, the location of LCFS is determined from the equilibrium reconstruction code EFIT, which is known to have limited precision. We will assume that the possible imprecision of the separatrix location is of systematic nature (at least in the range of studied discharges) [18] and we will focus on the relative changes of upstream quantities.

3. Effects of the seeding

3.1. Radiation measured by the visible cameras

The location of nitrogen injection is in the field of view of the rapid imaging system (RIS) [8]—a pair of fast color cameras operating in the visible range. The RIS1 camera was oriented with a tangential field of view of the plasma and

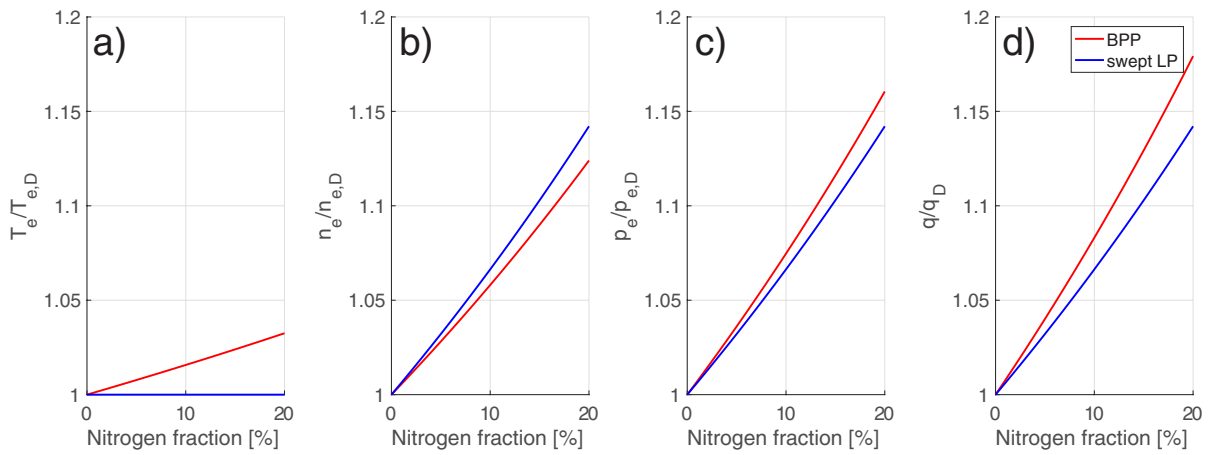


Figure 2. Imprecision of measurement of T_e (A), n_e (B) and p_e (C) for BPPs and LPs due to the presence of nitrogen in the plasma. All values are normalized to measurements in pure deuterium.

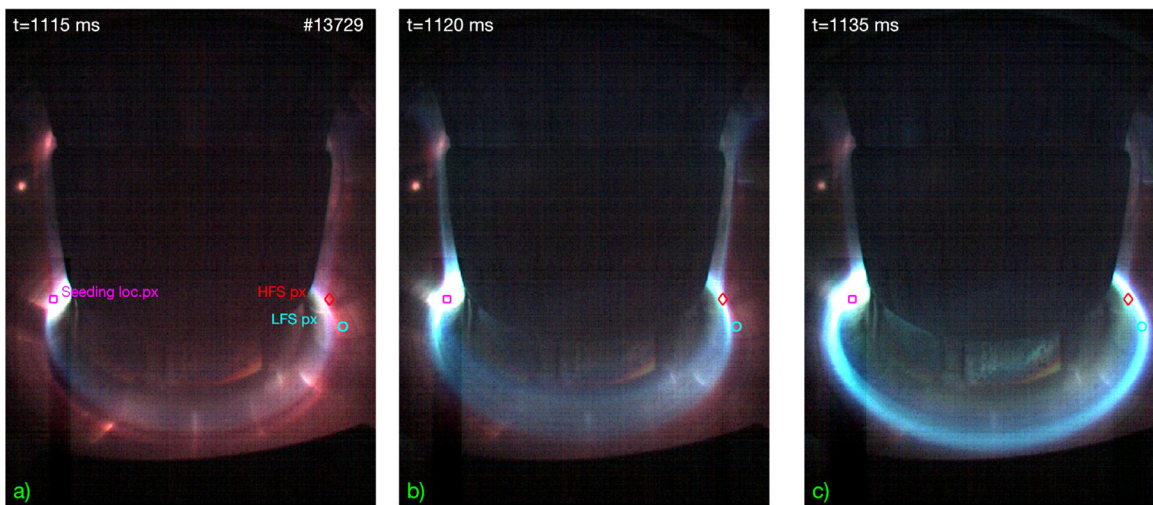


Figure 3. Three different patterns of nitrogen radiation in discharge #13729 ($\Gamma_{N_2} = 2.0 \times 10^{20} \text{ m}^{-3}$) observed by the RIS1 camera with marked locations of seeding, LFS and HFS pixels.

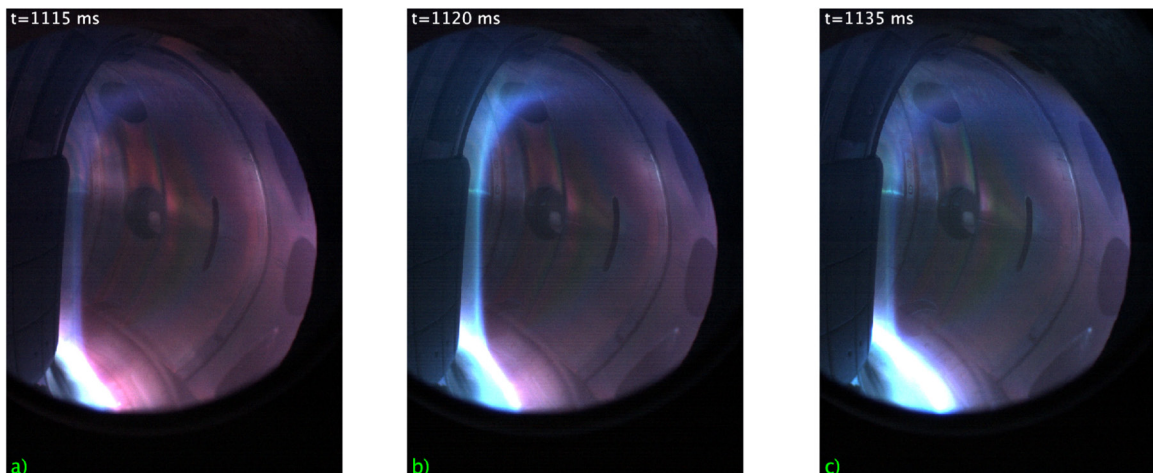


Figure 4. Three different patterns of nitrogen radiation in discharge #13729 observed by the RIS2 camera.

operated at a 8kHz sampling frequency with a resolution of 1280×624 RGB pixels, while RIS2 was providing a wide angle radial view at 5kHz and a resolution of 1280×1000 pixels. It was possible to identify three different patterns of

radiation during nitrogen injection, which are shown in figures 3 and 4. The piezoelectric valve was requested to be open at $t = 1100\text{ms}$ and after approximately 15ms it was possible to detect a new source of radiation around the injection

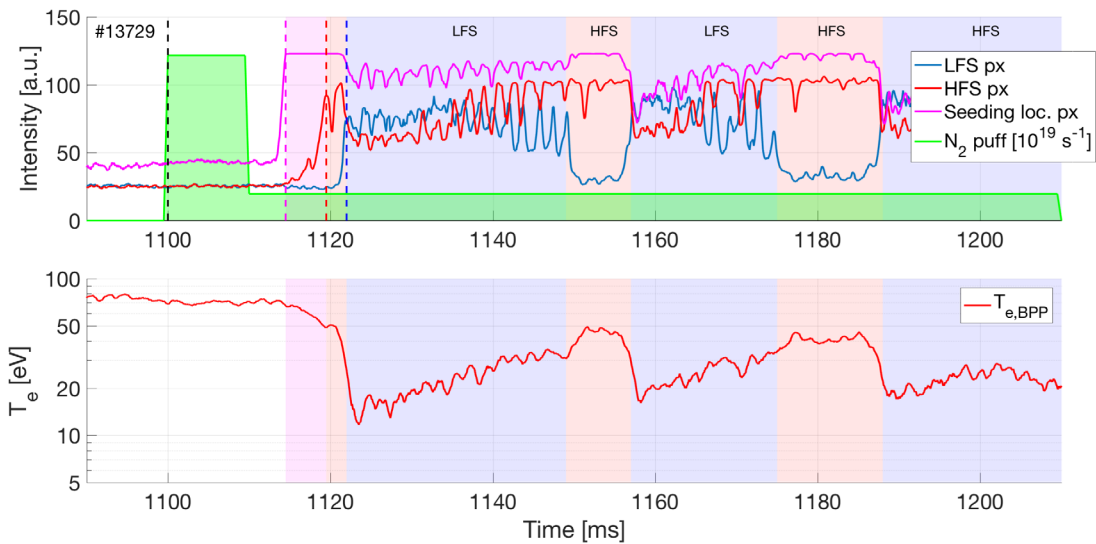


Figure 5. Pixel intensity at seeding location, HFS and LFS (top) and evolution of T_e at LFS target (bottom). Background colors and labels indicate radiation regimes shown in figures 3 and 4.

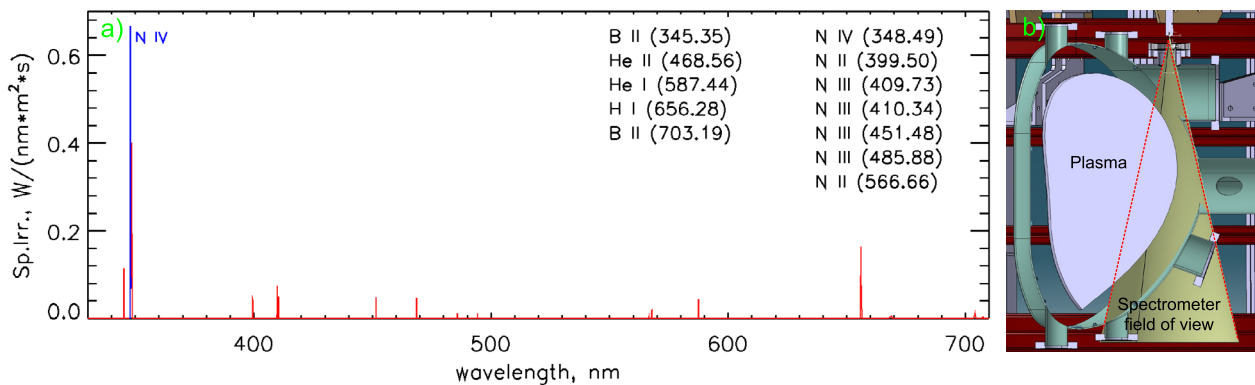


Figure 6. Nitrogen lines identified in the measured spectrum in discharge #15976 at $t = 1150$ ms (a) and the field of view of the minispectrometers (b).

location (figure 3(A)). Later, this radiation became more toroidally uniform but was restricted to the HFS (figure 3(B)), even in the cases when the injection was located at the outer strike point. In addition, measurements by the second RIS camera (see figure 4) show that the radiation is not limited to the inner target but extends up to the whole HFS SOL. In some discharges, where the amount of injected nitrogen was sufficient, there was an abrupt change of the radiation pattern and the radiation became centred around the x-point region (figure 3(C)). This transition was accompanied by a sudden change of temperature measured by the divertor probes, as shown in figure 5, for the discharge #13729 (HFS seeding $\Gamma_{N_2} = 2.0 \times 10^{20} \text{ s}^{-1}$), where several such transitions were observed, since the amount of injected nitrogen was probably marginal with respect to the detachment access. The pixel signal intensities (the total intensity from RGB channels was used) indeed follow this behaviour (patterns are labeled HFS and LFS in the figure) and sometimes exhibit low-frequency oscillations ($f \sim 1$ kHz), which according to RIS data are axisymmetric and resemble those measured at AUG [29]. For the definition of T_e plotted in figure 5 see section 3.4.

3.2. Spectroscopy measurements

The radiation of nitrogen was measured using a set of minispectrometers for near UV (247–473 nm), visible (460–663 nm), and infra-red (630–680 nm) ranges with resolutions of 0.15, 0.17, and 0.23 nm, respectively [25]. The field of view covers the edge plasma at the outer midplane but excludes the outer target, as shown in figure 6(B). It was possible to identify several nitrogen lines in the measured spectrum (see figure 6(A)). The most intensive line was measured in the near UV to blue visible spectrum was the N IV multiplet lines near 348 nm, with much weaker contributions from the N III multiplet lines near 410 nm and the N II singlet line at 399.5 nm. The qualitative behaviour of the N IV multiplet intensity follows the increase of radiated fraction $f_{\text{rad}} = P_{\text{rad}}/P_{\text{ohm}}$ (where P_{rad} is the total radiated power measured by bolometry [7] and P_{ohm} is the ohmic input power), as shown in figures 7(A) and (B).

We use line-of-sight in the axis of the field of view cone and select the time slice near the beginning of the N₂ seeding window ($t = 1150$ ms) in shot #15976 to discuss the model and necessary assumptions for estimating the N concentration

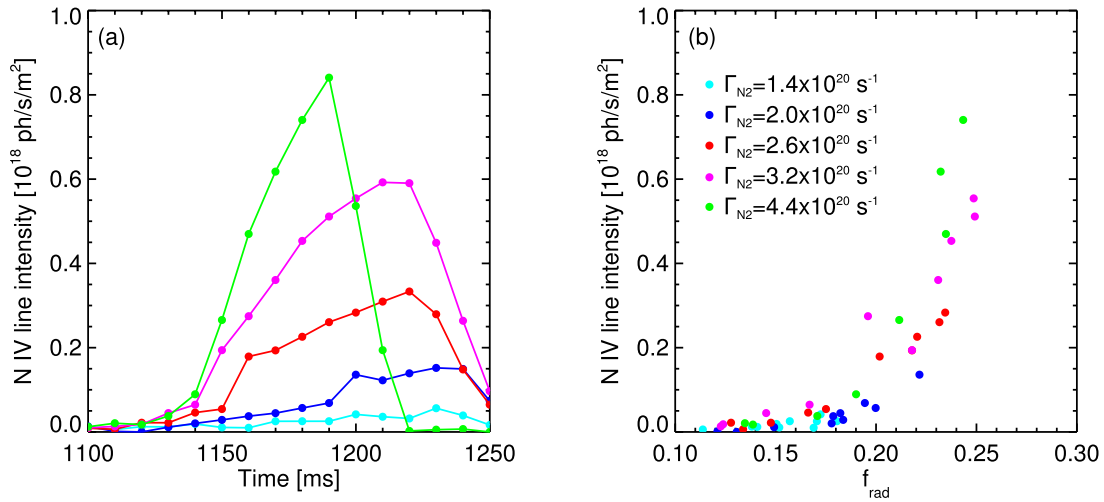


Figure 7. The intensity of the N IV multiplet line at 348 nm evolving in time (a) and as a function of radiated fraction f_{rad} (b).

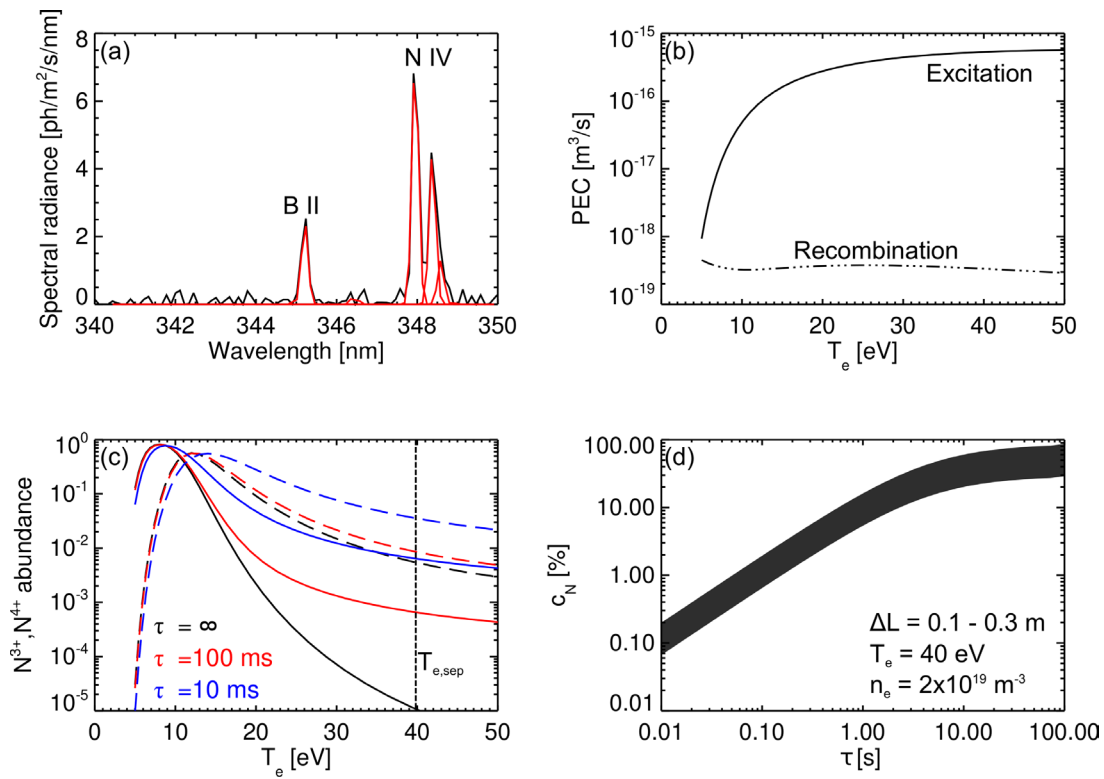


Figure 8. The measured spectral radiance (black) with Gaussian fit components (red) measured in the near UV for shot #15976 at $t = 1150$ ms is shown in (a). Excitation and recombination rates for the N IV multiplet transition at $\lambda \sim 348$ nm are shown as a function of T_e for $n_e = 2 \times 10^{19}$ m⁻³ in (b). The ion fractions of N^{3+} (solid) and N^{4+} (dashed) are shown in (c) for three different impurity residence times. The N concentration at $T_e = 40$ eV is shown as a function of τ in (d).

based on the N IV multiplet intensity. The N concentration, c_N , can be calculated using:

$$c_N = \frac{I_{N\ IV}}{f_{N^{3+}} PEC^{exc} + f_{N^{4+}} PEC^{rec}} \frac{1}{\Delta L n_e^2} \quad (2)$$

where $I_{N\ IV}$ is the N IV multiplet intensity, $f_{N^{3+},4+}$ are the ion fractional abundances of the $Z = 3+, 4 + N$ ions, $PEC^{exc,rec}$ are the photon emissivity rate coefficients for excitation and recombination, and ΔL is the length of the N IV emitting region through the line-of-sight, which is approximated by

the distance over which the line-of-sight penetrates inside the separatrix.

Firstly, to calculate the N IV multiplet intensity, a 4-Gaussian fit of the N IV multiplet emission feature and a single Gaussian fit of the nearby B II line is carried out as shown in figure 8(A). Next, the excitation and recombination rates for this transition are obtained from the Atomic Data and Analysis Structure (ADAS) and interpolated as a function of temperature in figure 8(B). From high resolution Thomson scattering (HRTS) system [9] measurements at this particular

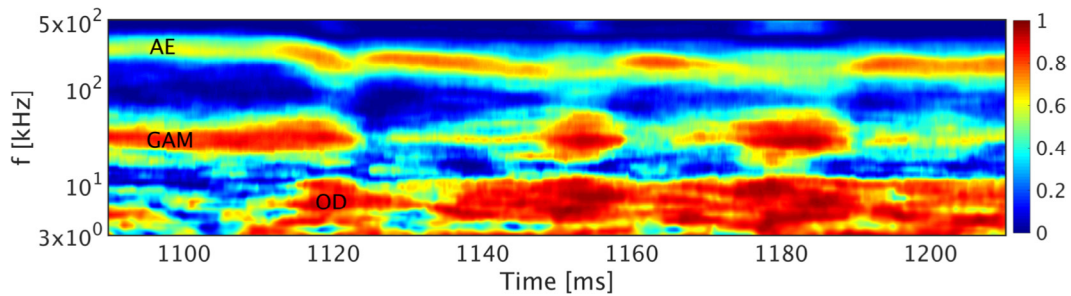


Figure 9. Wavelet cross-coherence between two Mirnov coils (MC17 and MA17), toroidally separated by 135° and located in the HFS divertor region of COMPASS (#13729).

time slice and shot, the separatrix density is $n_{e,sep} \sim 2 \times 10^{19} \text{ m}^{-3}$, while the temperature is $T_{e,sep} \sim 40 \text{ eV}$. The fractional abundance of the $\text{N}^{3+,4+}$ charge states are then calculated using an ionisation balance with a transport loss term, $n_e \tau$, where τ is the impurity residence time in the separatrix. This parameter is not well known in the separatrix, or indeed anywhere in the SOL; however, one could begin by estimating it using the typical particle confinement times which range from 5–15 ms in COMPASS. In theory, this parameter could also account for enhanced recombination due to neutral deuterium atoms in the separatrix. For this study, the ion fractions for three τ values of 10, 100, ∞ ms are shown in figure 8(C) by the red, blue, and black lines, where the solid and dashed lines represent the N^{3+} and N^{4+} charge states, respectively. The latter τ value represents the zero-transport case where only ionisation and recombination rate coefficients from ADAS are considered.

The c_N calculated at $T_{e,sep} = 40 \text{ eV}$ is shown in figure 8(D) as a function of τ . The shaded region shows the upper and lower limit of $\Delta L = 0.1\text{--}0.3 \text{ m}$. The c_N is unphysically high (close to 100%) in the zero-transport case ($\tau > 10 \text{ s}$) suggesting that transport must be included. Between $\tau = 10\text{--}100 \text{ ms}$, the c_N varies from 0.1–1.0% in the separatrix, which is likely a lower limit on the divertor nitrogen concentration since the ratio of the nitrogen concentration in the divertor and core plasma volumes has been observed on AUG to reach values of 10 [30]. These first results therefore provide a first insight into the divertor N concentrations required for detachment on COMPASS, however additional spectrometer sight-lines isolating the emission from the divertor volume (e.g. following the analysis of [31]) and core CX measurements of the nitrogen density would help to validate these estimations.

3.3. Magnetic measurements

COMPASS is equipped with two sets of non-integrated Mirnov coils toroidally separated by 135° , each composed of 24 coils located in the same poloidal cross section (see figure 1 in [33]) that allow studies of the poloidal magnetic field generated by instabilities that take place during the discharge duration. In figure 9, we present the wavelet cross-coherence between the two toroidally separated Mirnov coils 17, located in the HFS divertor region of COMPASS, that shows different instabilities during a nitrogen seeding experiment. One can observe that the MHD activity is strongly influenced by the nitrogen

injection. Related to the first temperature drop ($\sim 1120 \text{ ms}$), a strong mode develops around 6 kHz (labeled OD as onset of detachment) and grows back every time the transition between attached and detached plasma occurs (~ 1155 and 1187 ms). The geodesic acoustic mode [33] (labeled GAM around 30 kHz) also strengthens during every onset of detachment while the Alvfen eigenmode [34, 35] (labeled AE around 250 kHz) is damped. Between each divertor temperature drop, the GAM almost fully disappears while the AE mode builds up but with a lower frequency than prior to nitrogen seeding.

In nitrogen seeding experiments during H-mode operation [29] and also in density ramp-up L-mode operation [36] on the ASDEX Upgrade device, strong fluctuations around 6 kHz were observed by the AXUV (absolute extended ultraviolet) detectors near the x-point during the transition from attached to completely detached plasma. This phase called by the ASDEX team the *fluctuating detachment state* [37] may be linked to the development of the current convective instability [38]. As described in [38–40], such an instability develops when a large temperature difference exists between the inner and outer divertor, i.e. when the inner divertor detaches, as it usually detaches prior the outer one. Once the outer divertor detaches too, the temperature difference vanishes and the instability stabilises, so that the fluctuations disappear.

The mode visible around 6 kHz in figure 10 seems to have a similar behaviour as the fluctuating detachment state described above since it appears mainly during the temperature drop in the divertor region. In addition, AXUV detectors looking near the X-point region also detect these fluctuations indicating that they take place at this location. Studies of the toroidal mode number with Mirnov coils show that the mode is toroidally symmetric. Lastly, the signals coming from the different poloidally separated Mirnov coils seem to indicate that the instability is mostly present in the divertor region (coils 16–21) but also in the top part of the vessel (coils 5–10).

In figure 10, we show the coherence between the Mirnov coil MC17 and T_e in the outer divertor measured by the combination of Ball-pen and Langmuir probes at $R = 483 \text{ mm}$. The mode is strongly visible at the onset of detachment when the mean T_e significantly drops. The fluctuations are also visible in the HFS divertor since the coherence between MC17 and a floating potential measurement near the HFS strike point shows a similar picture as shown in figure 9. The density, however, does not show any such fluctuations

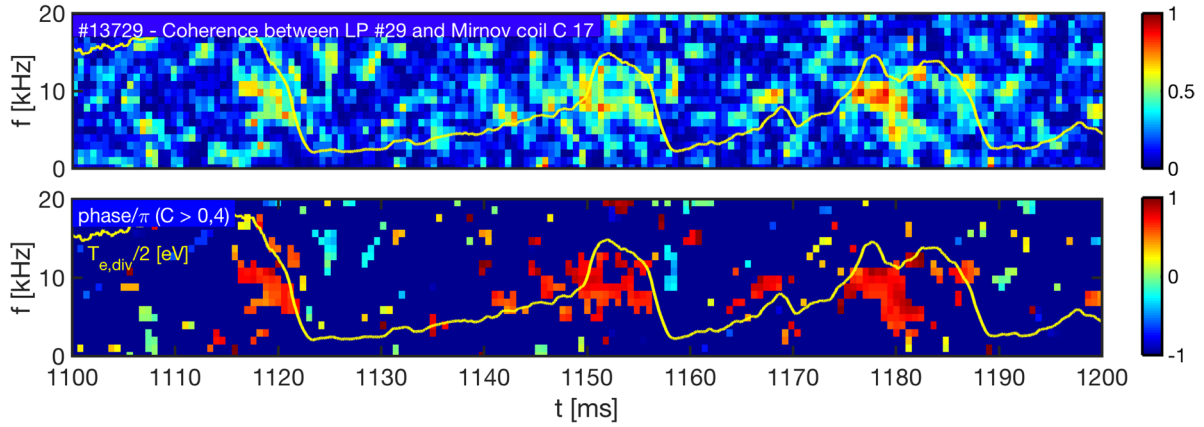


Figure 10. Coherence measurements: cross-coherence between T_e measurement near the LFS strikepoint of #13729 and the Mirnov coil MC17 (A) and associated phase divided by π (B). Yellow line indicates T_e measured by div. probes (divided by factor 2).

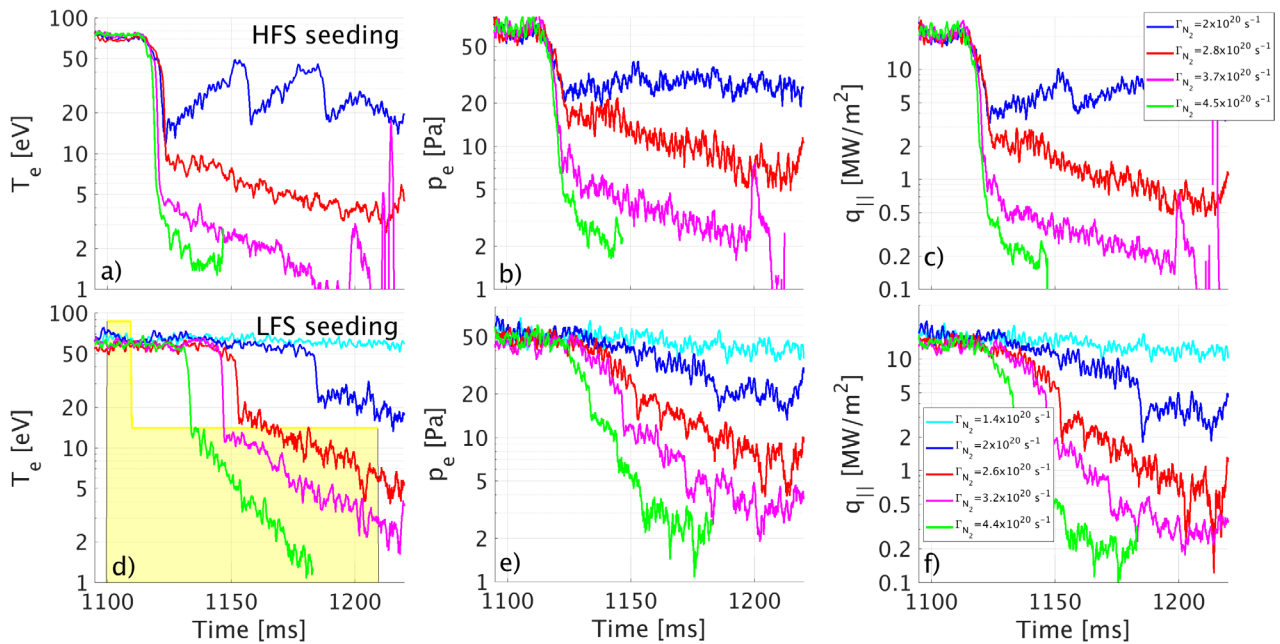


Figure 11. Temporal evolution of T_e , p_e and $q_{||}$ in the divertor for seeding at HFS ((a)–(c)) and LFS ((d)–(f)) measured by probes in the vicinity of the outer strike point.

in both HFS and LFS indicating that the process is mainly linked to the temperature, supporting the physical picture described by [38].

3.4. Effects in the divertor

Figure 11 summarises the effects of nitrogen seeding on the divertor temperature, pressure and heat flux, as measured by the combination of Langmuir and Ball-pen divertor probes. The values plotted in the figures correspond to the maximum quantities within 2 cm outside the OSP. The electron pressure was calculated as

$$p_e = (1 + M^2)n_e T_e, \quad (3)$$

where M is the parallel Mach number, which was assumed to be equal to 1 at the target due to the Bohm condition and equal

to 0 upstream. The heat flux was calculated from the measured values of T_e and j_{sat} . For simplicity it was assumed that the tiles were in ambipolar condition and so the parallel heat flux can be calculated as

$$q_{||} = (\gamma T_e + E_i)j_{\text{sat}}. \quad (4)$$

Where E_i is the potential energy deposited by each ion–electron pair to the target, which is equal to a sum of ionisation energy (13.6 eV for deuterium) and surface bonding energy (~ 1 eV) [42]. The value of the sheath heat transmission coefficient γ depends on the ratio T_i/T_e and the coefficient of secondary emission [11]. We assume that the secondary emission is negligible due to the small angle of incidence of the field lines with respect to the tile top surface (1 – 3°) [12]. Following the recent comparison with divertor IR measurements [41], we adopt a value of γ equal to 11, which corresponds to $T_i/T_e \sim 2.5$. Note

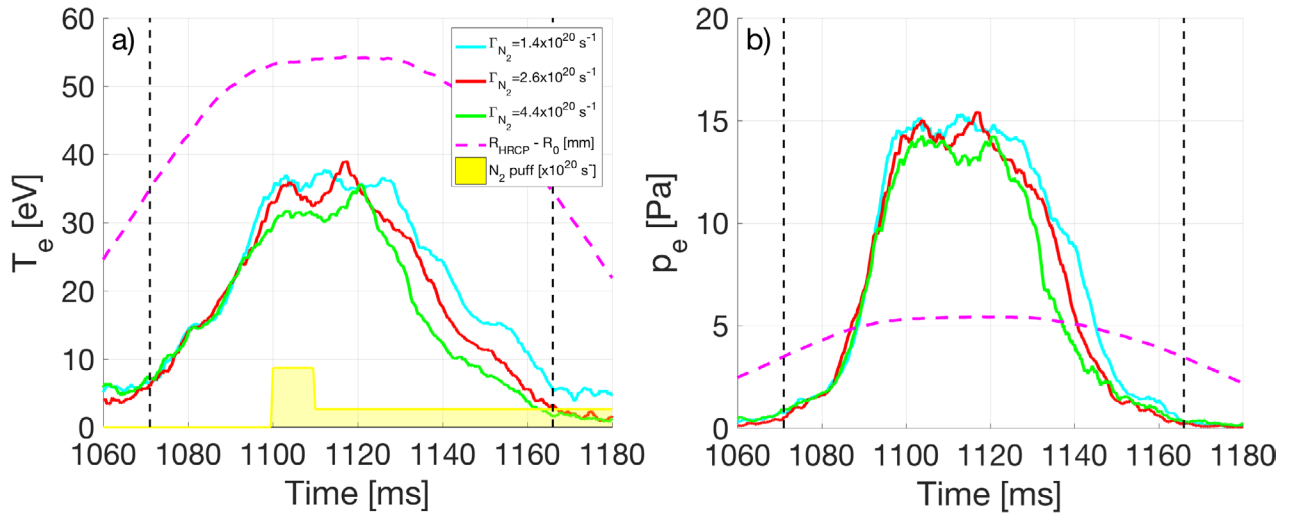


Figure 12. Time evolution of T_e and p_e during the movement of the HRCP. The vertical dashed lines indicate times where the probe penetrated beyond the limiter shadow.

that our analysis concentrates on such properties of the heat flux profiles, which are not affected by a possibly different value of γ , as long as it is constant along the target.

The effects of the impurities are dependent on the location of the seeding. When the impurity was introduced at the HFS, it was always followed by an abrupt change of temperature (figure 11(A)) at the outer target, similar to the behaviour which was observed at DIII-D [20]. For the highest amount of seeding, the discharge was ended prematurely due to a disruption caused by mode locking of a tearing mode.

When the nitrogen was seeded at the LFS, the effects in the divertor were generally more gradual (figures 11(d)–(f)). The abrupt response on the T_e is still present but the relative magnitude of the drop is smaller and occurs at different times depending on the amount of nitrogen influx. At low seeding values there are no relaxations observed (unlike the case of HFS seeding, as shown in figures 11(a)–(c)), instead the target pressure and heat flux only gradually decrease. At the highest level of seeding there is still a disruption but it occurs only at the end of the flat-top phase of the discharge.

3.5. Upstream and core parameters

Due to the proximity of the seeding location to the X-point and the relatively low edge plasma temperatures in ohmic plasmas, it was expected that some of the injected nitrogen may penetrate into the confined plasma and cool it by radiation. As a consequence, a pressure drop would be observed on the upstream profile. This was confirmed by measurements performed by the horizontal reciprocating manipulator equipped with the probe head featuring a combination of BPPs and LPs [19]. The probe head was only allowed to probe the far SOL to avoid possible perturbation of the divertor measurements. The position of the LCFS according to the EFIT reconstruction was at $R = 0.728$ m, so the probe head was about 2 cm ($\sim 2 \lambda_p$) away from the LCFS during the deepest point of reciprocation. Note that the radial position of the probe R_{hrcp} in figure 12 is plotted relative to the parking position

$R_0 = 800$ mm. The probe was moving during the discharges with seeding at the LFS at such timing that the inward motion was performed before the beginning of seeding, while the outward movement occurred during the seeding. Unfortunately the effect of nitrogen upstream was gradual over the duration of the movement (see e.g. figures 11(d)–(f)), and so it was not possible to extract a true radial profile of the measured quantities during the outward motion. However, the time evolution of T_e and p_e as shown in figure 12 demonstrate a reduction of both quantities during the outward motion, depending on the amount of injected nitrogen. The electron pressure was calculated as in equation (3). The density was deduced from the measurement of the ion saturation current of a Langmuir pin assuming $T_i/T_e = 2$ and the effective collecting area given by a recently developed model [17].

Another indication of the radiation in the confined plasma is provided by measurements of the radiation in the confined plasma is provided by measurements of power dissipated by radiation inside the LCFS $P_{rad,insep}$, which is calculated by tomographic reconstruction of the AXUV bolometers measurements [7]. Also, measurements of the ohmic power P_{ohm} , obtained by magnetic measurement of U_{loop} , should show an increase due to higher Z_{eff} caused by the presence of nitrogen. Both effects are easily visible in the profiles presented in figure 13. Note that in #15976 (magenta line in figure 13(A)), the initial radiation was significantly higher than in the other discharges in the scan, however the relative change which occurred after the beginning of seeding is in line with the trends observed in other discharges.

3.6. Upstream and downstream pressure

The findings presented during the previous section cast doubts over whether the pronounced change in divertor parameters is due to nitrogen radiating in the SOL or whether the whole edge plasma is cooled. In order to distinguish between these two possibilities, the measurements of upstream and downstream pressures were compared. While the change of peak electron pressure at the outer target was measured using the

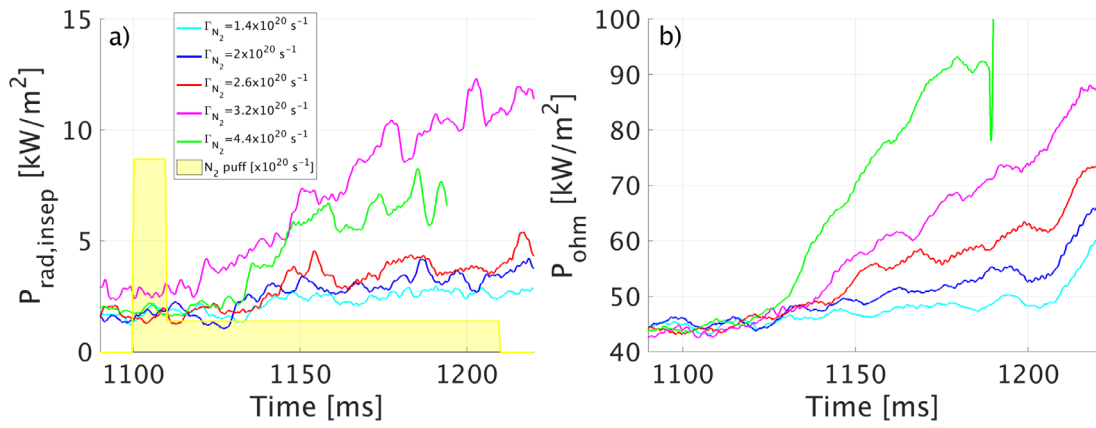


Figure 13. Time evolution of the plasma radiation measured by AXUV bolometers (left) and measurements of ohmic power P_{rad} .

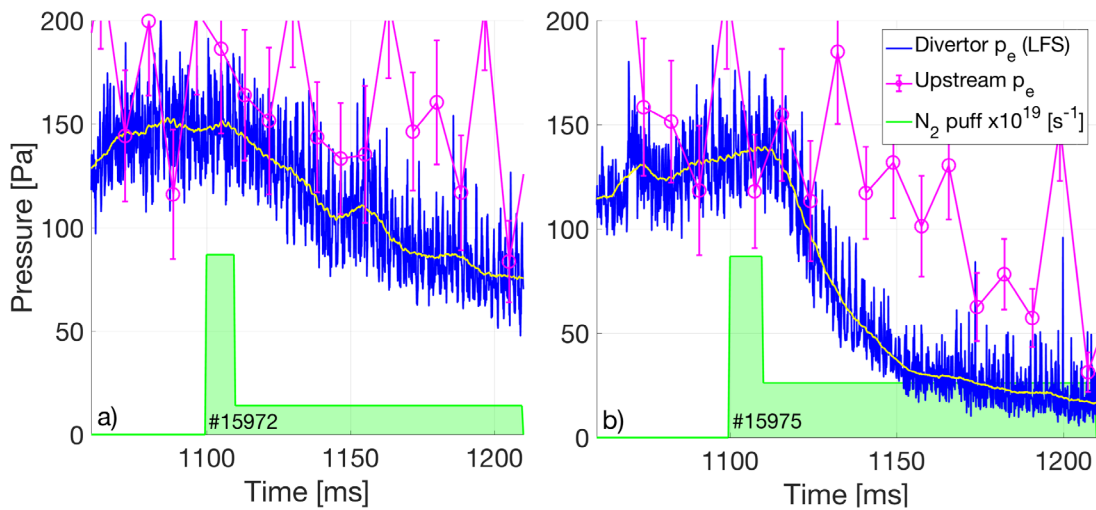


Figure 14. Evolution of upstream (magenta) and downstream (blue) pressure in discharges with low $\Gamma_{\text{N}_2} = 1.4 \times 10^{20} \text{ s}^{-1}$ (A) and high $\Gamma_{\text{N}_2} = 3.2 \times 10^{20} \text{ s}^{-1}$ (B) amount of seeding.

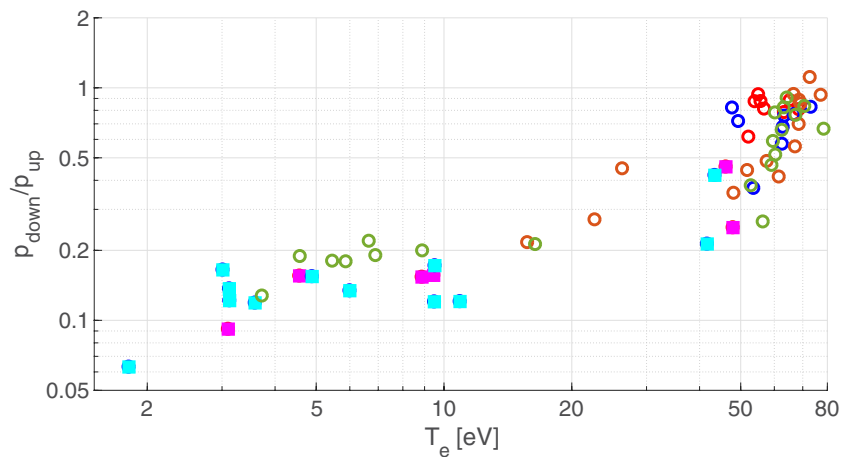


Figure 15. Ratio of downstream (p_{down}) and upstream (p_{up}) pressures as a function of maximum T_e at the outer target in different discharges with LFS nitrogen seeding. Square symbols indicate application of NBI.

LP and BPP divertor probes, the upstream pressure was monitored by HRTS [9] at the position of the separatrix calculated by magnetic reconstruction. Both upstream and downstream pressures were calculated using equation (3).

It was observed that there is a significant drop of the downstream pressure following the injection of nitrogen and that

the speed of the response and the magnitude of the pressure drop can be controlled by the amount of injected nitrogen, as shown in figure 14. As expected, the effect of nitrogen was not restricted to only the divertor but also affected the upstream pressure. When this pressure drop (visible e.g. in figure 14(B)) was taken into account, it became difficult to

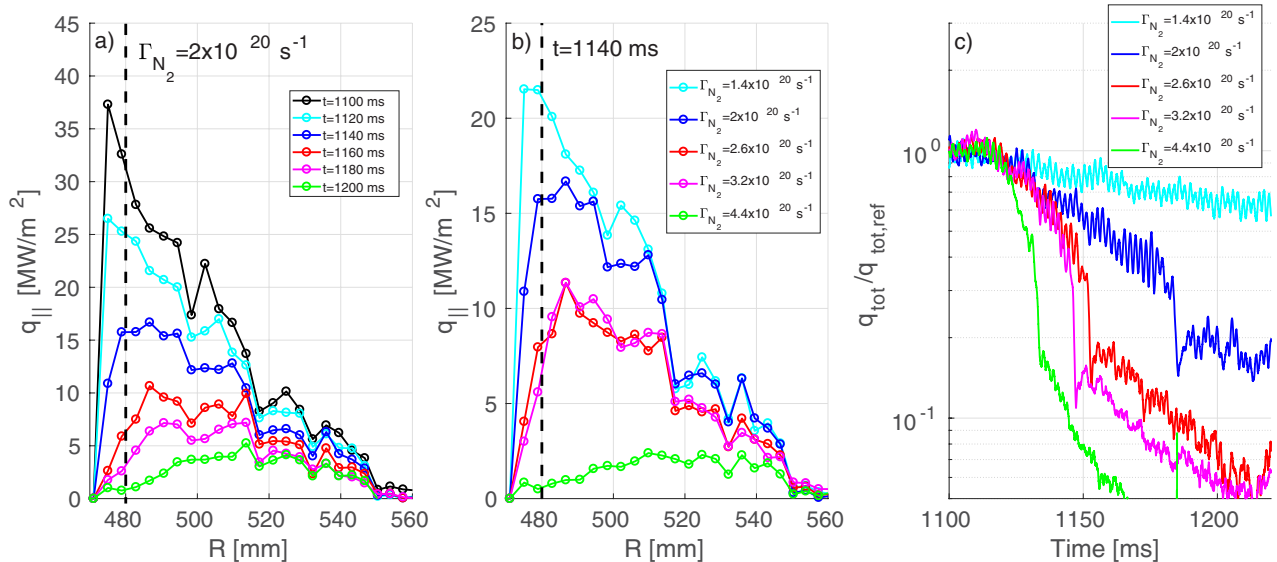


Figure 16. Temporal evolution of heat flux during a seeding experiment in the vicinity of the outer strike point (a), heat flux profiles at $t = 1140$ ms for varying amounts of seeding (b) and the ratio of integral heat flux at the outer target q_{tot} normalized to pre-seeding levels $q_{\text{tot,ref}}$ (c).

determine whether the effect of nitrogen in the SOL is more significant than in the confined region.

In order to resolve this issue, a new set of experiments was performed, where the effect of nitrogen radiation inside the separatrix was compensated with the application of NBI heating. The effect of auxiliary heating on the upstream profiles was expected to be only moderate, so the maximum available power of 450 kW was delivered into the plasma at $t = 1120$ ms (the beginning of the seeding waveform was shifted to $t = 1080$ ms in these discharges). Note that in a non-seeded discharge this would lead to access to the H-mode but the presence of nitrogen clearly prevents it.

The achieved pressure drop is summarised in figure 15, where the ratio of the downstream and upstream pressures in all discharges with LFS nitrogen seeding is plotted against the target temperature. The lowest pressure fractions were achieved during the NBI phases (marked by squares in the figure) and represent a clear demonstration of partial detachment. Note that the shape of the dependency on T_e is quite different than that observed at C-mod [21] and AUG [22]. This can be a consequence of the radiation of nitrogen in the confined plasma, which is not so detrimental in larger devices.

4. Buffered heat flux at the outer target

The principal objective of operation in the detached regime is to mitigate heat fluxes impinging onto the divertor targets, in order to avoid damage of the PFCs. This is already needed in some of the contemporary machines (such as AUG) in high-power scenarios and it will be unavoidable for ITER and other next-step machines. In order to evaluate the effect of impurity seeding on the heat fluxes, the radial profiles of heat flux were constructed based on probe measurements at the outer targets using equation (4).

Figure 16 summarises the heat flux measurements, with data from discharges, where nitrogen was introduced at the LFS. The impurity injection causes a large decrease of the heat flux close to the strike point (marked by vertical dashed line), reducing it by more than a factor of 10, while further away the reduction is less significant.

Instead of attempting to characterise directly the heat flux footprints during nitrogen seeding, one can use the attached heat flux profile as a reference q_{ref} (black line in figure 16(A)) and introduce a buffered heat flux q_B , the heat flux which has been removed from the footprint due to the presence of the injected impurity:

$$q_B(t, R) = (q_{\text{ref}}(R) - q(t, R))/q_{\text{ref}}(R). \quad (5)$$

Since the effect of the nitrogen seeding is believed to be localised in the divertor region, we prefer not to map the profiles to the outer midplane but instead use the radial coordinate R at the target. An example of the profiles of buffered flux q_B in the case of moderate seeding at the LFS are shown in figure 17(A). The profiles can be well characterised by an exponential decay

$$q_B(R) = A_B \exp(-(R - R_{\text{OSP}})/\lambda_B). \quad (6)$$

Due to the limited data set it is difficult to determine if the exponential dependency is the best fit of the decay, as it is neither backed by any hypothesis regarding the underlying physical processes. However, it allows us to characterise the main features of the buffering: the magnitude of buffering at the strike point A_B and the spatial extent of the buffering λ_B . Note that the values of λ_B are significantly larger than the λ_q in the attached plasmas (typically between 20–40 mm at the outer target).

These parameters are expected to be primarily dependent on the inventory of nitrogen in the plasma and the consequent radiation losses. Indeed, both parameters exhibit strong

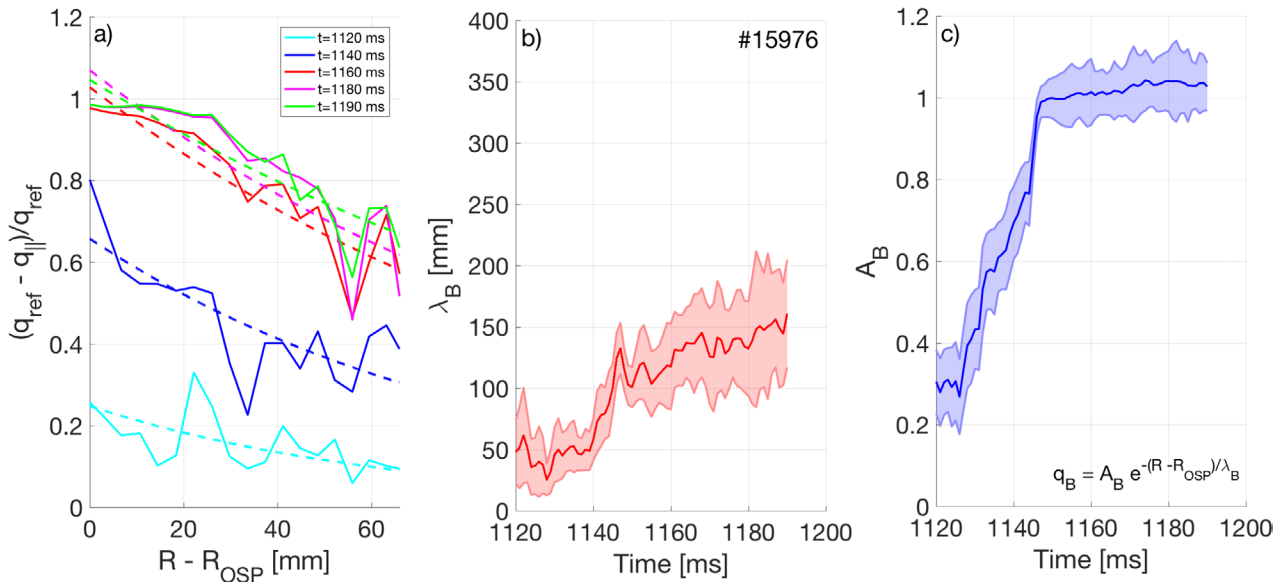


Figure 17. Buffered heat flux during discharge #15976 (A) and the time evolution of the fitting parameters λ_B (B) and A_B (C).

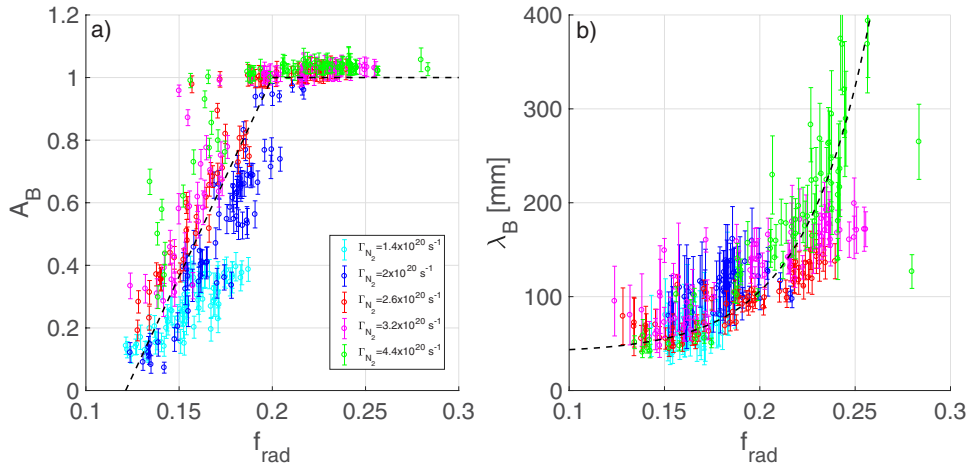


Figure 18. Dependence of buffer fit parameters A_B (left) and λ_B (right) on the radiated fraction in the discharge.

dependencies on f_{rad} , as shown in figure 18. While the evolution of the parameter A_B can be characterised by a linear increase for $0.1 < f_{\text{rad}} < 0.2$, λ_B also continues to increase further for higher values of f_{rad} with an approximately exponential dependence. Only fits with errors lower than 50% were used for this analysis, which discarded a number of fits at low f_{rad} in particular. In such cases the buffering of heat fluxes is small and so the q_B is subject to higher levels of fluctuations.

5. Characterisation of the partially detached divertor footprints

The divertor heat fluxes in attached conditions are typically mapped to the outer midplane and characterised by a function proposed by Eich in [23], which is a convolution of an exponential decay (with power decay length λ_q) and the Gaussian broadening of the profile (with characteristic width S) given by

$$q_s = \frac{q_0}{2} \exp\left(\left(\frac{S}{2\lambda_q}\right)^2 - \frac{s}{\lambda_q f_x}\right) \cdot \text{erfc}\left(\frac{S}{2\lambda_q} - \frac{s}{S f_x}\right) + q_{\text{BG}}, \quad (7)$$

where f_x is the flux expansion at the target, q_0 the peak heat flux, q_{BG} the background heat flux due to radiation and s is the spatial coordinate running along the target in the poloidal direction. This function reflects the assumption that the divertor target profile is partially determined by upstream conditions (exponential decay) and partially by processes in the divertor region (collisions and finite Larmor effects [13]). With respect to the spatial extend of the power deposition, the footprint can be approximated by an exponential decay with characteristic *integral power decay length* λ_{int} [24]

$$\lambda_{\text{int}} = \lambda_q + 1.64S. \quad (8)$$

This characterisation proved to be successful for the accurate description of heat flux profiles on a number of machines [23]. However, its domain of applicability is limited by the

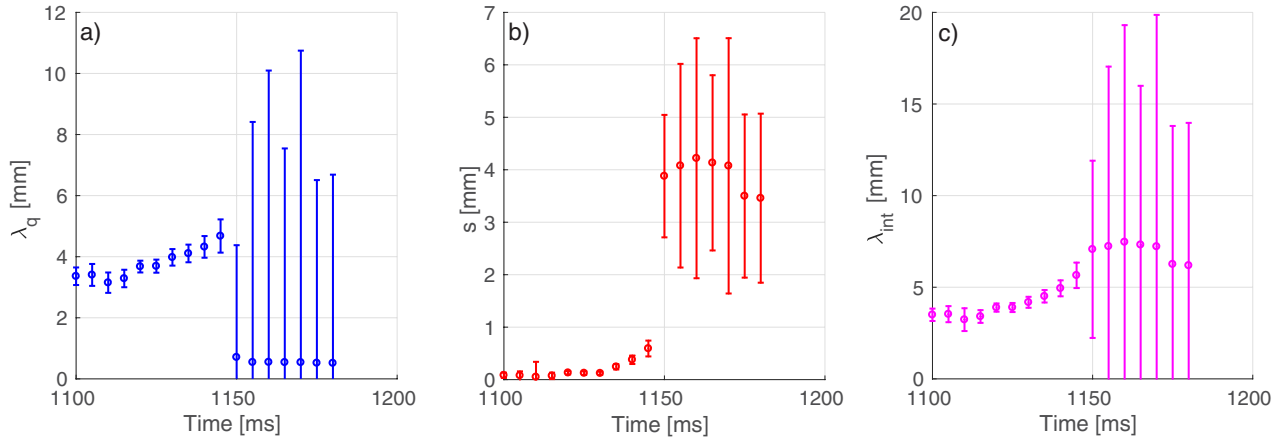


Figure 19. Time evolution of λ_q (A), s (B) and λ_{int} (C) in shot #15976.

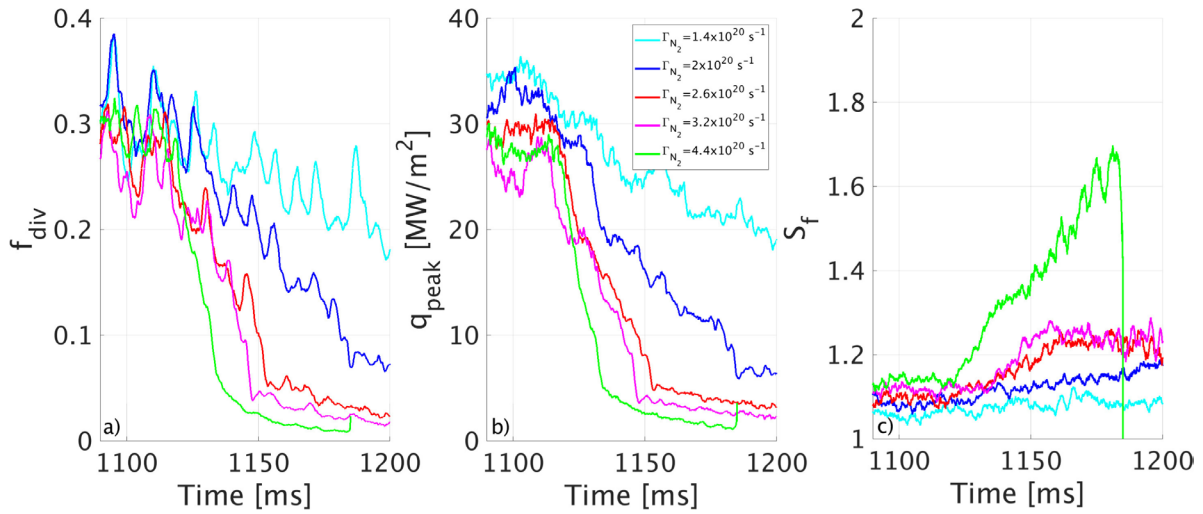


Figure 20. Time evolution of f_{div} (A), q_{peak} (B) and S_f (C) in discharges with LFS nitrogen seeding.

physical picture described above, which does not include, for example, dissipative processes, where part of the power is converted into radiation. With 5 degrees of freedom available, the formula 7 can still be technically applied to fit the target profiles even when such processes are significant (as it is the case in detached plasmas) but in such cases the fitting parameters λ_q and S lose their original meaning. In order to illustrate this, we have analyzed discharge #15976 ($\Gamma_{\text{N}_2} = 4.4 \times 10^{20} \text{ s}^{-1}$) and plotted the time evolution of λ_q , S and λ_{int} in figure 19. It can be seen that the fitted λ_q is increasing during the initial part of the seeding until the transition to detachment (around $t = 1150 \text{ ms}$), when it sharply drops and the quality of the fit significantly decreases. However, the main parameters which determine the fit according to L-mode multi-machine scaling by Eich [32] (B_T and q_{cyl}), remain constant during the flat-top. The apparent change of λ_q is a consequence of different physical processes influencing the divertor footprint—the effect of nitrogen seeding has a different nature than a Gaussian broadening of the profile.

In order to analyse the profiles in detached plasmas (as shown in figures 16(A) and (B)), a new set of parameters should be implemented to allow multi-machine comparisons. The approach presented in the previous section is feared to

be limited to particular conditions of the COMPASS divertor and may not be applicable on other tokamaks. Since the problem of heat fluxes is mostly an engineering issue, we propose to characterise the heat fluxes by a set of parameters, which are suitable for the evaluation of safety issues related to PFCs. These are the following: (i) *peak heat flux* q_{peak} being the maximum of heat flux (from which the background radiation q_{BG} is subtracted), (ii) *divertor power fraction* $f_{\text{div}} = 2\pi R \int q_{\parallel}(s) \sin(\alpha(s)) ds / P_{\text{sep}}$ being the fraction of power crossing the separatrix which reaches the target and (iii) *footprint spreading factor* S_f , which is the minimal distance along the target over which $1 - 1/e \sim 63\%$ of the power is deposited, normalized by the expected footprint width in an idealized case of attached plasmas in the absence of spreading ($S = 0$) $\lambda_q f_x$.

In the case of attached plasmas with a constant angle of incidence α , one can relate the new set of parameters with those implemented by Eich:

$$q_{\text{peak}} = q_0 \frac{\lambda_q}{\lambda_{\text{int}}}; f_{\text{div}} = 2\pi R f_x q_0 \lambda_q \sin(\alpha) / P_{\text{sep}};$$

$$S_f = \lambda_{\text{int}} / \lambda_q = 1 + 1.64 S / \lambda_q. \quad (9)$$

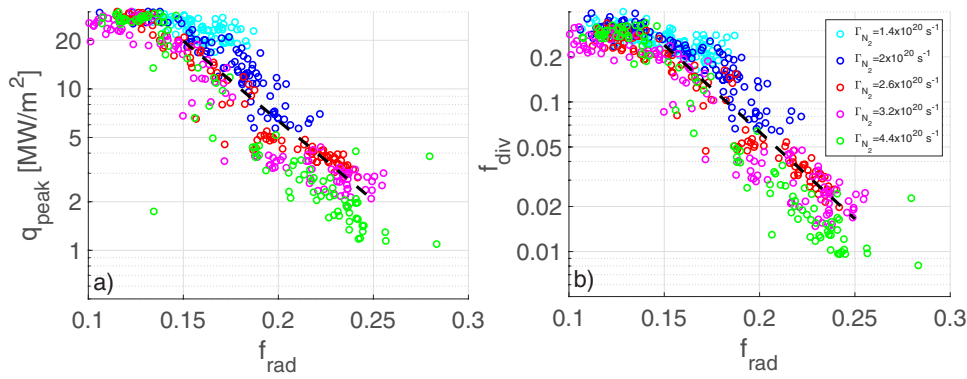


Figure 21. Dependence of parameters q_{peak} and f_{div} on the radiated fraction f_{rad} .

Time traces shown in figure 20 show the evolution of the new set of parameters obtained at the outer target. It can be seen that while f_{div} and q_{peak} are changing dramatically during the impurity seeding, the third parameter S_f shows a significant increase only for the highest seeding rate.

As with the parameters describing the buffered heat flux, it is again expected that the main factor influencing their evolution is the nitrogen radiation in the plasma. The dependencies (shown in figure 21) confirm this expectation. Both q_{peak} and f_{div} are steadily decreasing as f_{rad} exceeds a threshold value of 0.15, with an approximately exponential dependence.

6. Comparison with the detachment scaling model

A recent model for detachment scaling introduced by Goldston [26] allows the prediction of the nitrogen concentration required for detachment. In order to compare COMPASS data with the results presented in [26], it is necessary to account for the fact that our experiments were performed in L-mode, where the power decay length is expected to be larger than in H-mode. Indeed, the heuristic drift model [27] predicts $\lambda_{q,HD} = 2.5$ mm, while analysis of the footprint at the outer target prior to seeding shows $\lambda_q = 4$ mm. In order to rescale the results obtained for AUG in [26], we need to calculate the factor $P_{\text{sep}}/((\lambda_q/\lambda_{q,HD})^{8/7} \langle B_p \rangle (n_{\text{sep}}/n_{\text{gw}})^2 I_{\parallel}^*)$, which has a value of 200 ($P_{\text{sep}} = 230$ kW, $\langle B_p \rangle = 0.16$ T, $n_{\text{sep}} = 1.7 \times 10^{19}$ m⁻³, $n_{\text{gw}} = 21.8 \times 10^{19}$ m⁻³, $L_{\text{con}} = 3.9$ m, $q_{\text{cyl}} = 4.2$, $I_{\parallel}^* = 0.54$). Using data from table 2 in [26], one finds the predicted impurity fraction $c_{z,\text{Goldston}} = 7.6\%$, which is higher than on JET or AUG but lower than the fraction predicted for ITER.

Unfortunately, the analysis of spectroscopy data does not allow for precise confrontation of this prediction. The estimation based on spectral measurements presented in section 3.2 allows only for rough comparison, since the key parameters τ and ΔL are not known with sufficient precision. Another rough estimate of nitrogen concentration can be obtained from the knowledge of the nitrogen seeding rate, which can deliver $1\text{--}4 \times 10^{19}$ particles into the vessel during the discharge. Given the approximate vessel volume of 1 m³ and the line-averaged density of 4.0×10^{19} m⁻³, the c_z would be 25%–100% if nitrogen was to be distributed uniformly and in the absence of

nitrogen removal mechanisms. This is clearly too high for the plasma to sustain operation.

The most realistic estimate can be obtained from calculations of the cooling power $P_{\text{cool}} = c_z n_e^2 L_z$, which as seen in figure 16 can compensate for almost the whole P_{sep} . The radiative loss function L_z can be approximately determined from figure 3 in [28] as 2×10^{-32} Wm³, which yields c_z of 5 percent, a value consistent with Goldston's prediction.

7. Conclusions

Measurements of plasma parameters in the COMPASS tokamak during nitrogen seeding were performed using a variety of diagnostics. The most important tool for the evaluation of plasma conditions in the divertor region was the combined array of Ball-pen and Langmuir probes. Despite persisting open questions in the evaluation of probe data in detached conditions, the relative changes of electron pressure and heat flux allowed the characterisation of the effects of nitrogen seeding.

Nitrogen seeding was proved to be an efficient tool for the reduction of divertor pressure and heat flux in a series of dedicated L-mode discharges at COMPASS. The plasma response to the seeding is in general dependent on the location of the seeding, with more favourable results being achieved from seeding in the vicinity of the outer strike point. The nitrogen radiation is not restricted to the divertor region but also affects the confined plasma, which results in a considerable upstream temperature drop. During the NBI-assisted discharges the ratio of upstream and downstream pressure changed by a factor of 10, which is a clear demonstration of partial detachment.

In order to characterise the effect of nitrogen seeding on the divertor footprint, the buffered heat flux q_B was introduced. The buffered heat flux at COMPASS can be approximated well by an exponential decay with large characteristic length. Both parameters describing q_B exhibit a strong dependence on the radiated fraction, however this feature remains to be tested on data from other machines. Also, a more generic way of characterising the heat fluxes was proposed, to answer the practical questions related to the engineering limits of the plasma-facing components. The peak heat flux q_{peak} and divertor power fraction f_{div} again depend strongly on the radiated fraction, however the footprint spreading factor S_f is

insensitive and remains constant during seeding in most of the discharges.

Acknowledgments

The first author would like to thank R.J. Goldston for valuable discussions related to his detachment scaling model and T. Eich for discussion on the λ_q scaling. This work has been carried out within the framework of the EUROfusion Consortium and has received funding from the Euratom research and training programme 2014–2018 and 2019–2020 under Grant agreement No. 633053. The views and opinions expressed herein do not necessarily reflect those of the European Commission. It was supported by projects Czech Science Foundation GA15-10723S, GA16-14228S, MYES projects #LM2015045 and CZ.02.1.01/0.0/0.0/16_013/0001/551 and IAEA CRP F13019—Research Contract No. 22727/R0.

ORCID iDs

S. Henderson  <https://orcid.org/0000-0002-8886-1256>

J. Horacek  <https://orcid.org/0000-0002-4276-3124>

M. Faitsch  <https://orcid.org/0000-0002-9809-7490>

J. Krbec  <https://orcid.org/0000-0002-3780-6257>

M. Peterka  <https://orcid.org/0000-0003-4352-8895>

References

- [1] Komm M. et al 2017 *Proc. of the 44th EPS Conf. (Belfast, UK, 26–30 June 2017)* P1.118 (<http://ocs.ciemat.es/EPS2017PAP/pdf/P1.118.pdf>)
- [2] Adamek J. et al 2017 *Nucl. Fusion* **57** 116017
- [3] Adamek J. et al 2016 *Rev. Sci. Instrum.* **87** 043510
- [4] Brunner D. et al 2016 *Nucl. Fusion* **58** 094002
- [5] Fevrier O. et al 2018 *Rev. Sci. Instrum.* **89** 053502
- [6] Ohno N. et al 2001 *Contrib. Plasma Phys.* **41** 473–80
- [7] Mlynar J. et al 2012 *Rev. Sci. Instrum.* **83** 10E531
- [8] Havranek A. et al 2017 *Fusion Eng. Des.* **123** 857–60
- [9] Aftanas M. et al 2012 *Rev. Sci. Instrum.* **83** 10E350
- [10] Eich T. et al 2018 *Nucl. Fusion* **58** 034001
- [11] Stangeby P.C. 2000 *The Plasma Boundary of Magnetic Fusion Devices* (Bristol: IOP Publishing)
- [12] Igitkhanov Yu. and Janeschitz G. 2001 *J. Nucl. Mater.* **99** 290–3
- [13] Sieglin B. et al 2016 *Plasma Phys. Control. Fusion* **58** 055015
- [14] Gunn J.P. et al 2017 *Nucl. Fusion* **57** 046025
- [15] Kukushkin A.S. et al 2009 *Nucl. Fusion* **49** 075008
- [16] Petrie T.W. et al 1997 *J. Nucl. Mater.* **241–3** 639–44
- [17] Podolnik A. et al 2018 *Plasma Phys. Control. Fusion* **60** 085008
- [18] Jirakova K. et al 2018 *Proc. of the 45th EPS Conf. (Prague, Czech Republic, 2–6 July 2018)* P5.1081 (<http://ocs.ciemat.es/EPS2018PAP/pdf/P5.1081.pdf>)
- [19] Adamek J. et al 2017 *Nucl. Fusion* **57** 022010
- [20] McLean A.G. et al 2015 *J. Nucl. Mater.* **463** 533–6
- [21] Lipschultz B. et al 2017 *Fusion Sci. Tech.* **51** 369–89
- [22] Perez I.P. et al 2017 *Nucl. Mater. Energy* **12** 182–6
- [23] Eich T. et al 2013 *Nucl. Fusion* **53** 093031
- [24] Makowski M.A. 2012 *Phys. Plasmas* **19** 056122
- [25] Naydenkova D. et al 2014 *Appl. Opt.* **53** 8123–30
- [26] Goldston R.J. et al 2017 *Plasma Phys. Control. Fusion* **59** 055015
- [27] Goldston R.J. et al 2012 *Nucl. Fusion* **52** 013009
- [28] Kallenbach A. et al 2016 *Plasma Phys. Control. Fusion* **58** 045013
- [29] Reimold F. et al 2015 *Nucl. Fusion* **55** 033004
- [30] Kallenbach A. et al 2017 *Nucl. Fusion* **57** 102015
- [31] Henderson S.S. et al 2018 *Nucl. Fusion* **58** 016047
- [32] Eich T. et al 2013 *J. Nucl. Mater.* **438** S72–7
- [33] Seidl J. et al 2017 *Nucl. Fusion* **57** 126048
- [34] Melnikov A.V. et al 2015 *Plasma Phys. Control Fusion* **57** 065006
- [35] Markovic T. et al 2017 *Proc. of the 44th EPS Conf. (Belfast, UK, 26–30 June 2017)* P5.140 (<http://ocs.ciemat.es/EPS2017PAP/pdf/P5.140.pdf>)
- [36] Potzel S. et al 2014 *Nucl. Fusion* **54** 013001
- [37] Potzel S. et al 2013 *J. Nucl. Mater.* **438** S285–90
- [38] Stepanenko A. et al 2018 *Phys. Plasmas* **25** 012305
- [39] Krasheninnikov S.I. et al 2017 *Nucl. Mater. Energy* **12** 1061–6
- [40] Krasheninnikov S.I. et al 2016 *Phys. Plasmas* **23** 092505
- [41] Vondracek P. 2018 Plasma heat flux to solid structures in tokamaks *Dissertation Thesis* Charles University, Prague (<https://is.cuni.cz/webapps/zzp/detail/123000/>)
- [42] Komm M. et al 2017 *Plasma Phys. Control. Fusion* **59** 094002
- [43] Silva C.S. 1999 *J. Nucl. Mater.* **266–9** 679–84
- [44] Meyer H. et al 2017 *Nucl. Fusion* **57** 102014